

Solar Atmosphere Wave Dynamics Generated by Solar Global Oscillating Eigenmodes

M. K. Griffiths

¹*Solar Physics and Space Plasma Research Centre (SP²RC), School of Mathematics and Statistics, University of Sheffield, Hicks Building, Hounsfield Road, S7 3RH, UK*

²*Corporate Information and Computing Services, The University of Sheffield, 10-12 Brunswick Street, Sheffield, S10 2FN, UK.*

³V. Fedun

³*Department of Automatic Control and Systems Engineering, The University of Sheffield, Mappin Street, Sheffield, S1 3JD, UK*

^{4,5}R. Erdélyi

⁴*Solar Physics and Space Plasma Research Centre (SP²RC), School of Mathematics and Statistics, University of Sheffield, Hicks Building, Hounsfield Road, S7 3RH, UK*

⁵*Department of Astronomy, Eötvös Loránd University, P.O.Box 32, Budapest, H-1518 Hungary*

⁶R. Zheng

⁶*Shandong Provincial Key Laboratory of Optical Astronomy and Solar-Terrestrial Environment, and Institute of Space Sciences, Shandong University, Weihai 264209, China*

Abstract

The solar atmosphere exhibits a diverse range of wave phenomena, where one of the earliest discovered was the five-minute global acoustic oscillation, also referred to as the *p*-mode. The analysis of wave propagation in the solar atmosphere may be used as a diagnostic tool to estimate accurately the physical characteristics of the Sun's atmospheric layers.

Email addresses: m.griffiths@sheffield.ac.uk (M. K. Griffiths), v.fedun@sheffield.ac.uk (³V. Fedun), robertus@sheffield.ac.uk (^{4,5}R. Erdélyi), r.zheng@sheffield.ac.uk (⁶R. Zheng)

In this paper, we investigate the dynamics and upward propagation of waves which are generated by the solar global eigenmodes. We report on a series of hydrodynamic simulations of a realistically stratified model of the solar atmosphere representing its lower region from the photosphere to low corona. With the objective of modelling atmospheric perturbations, propagating from the photosphere into the chromosphere, transition region and low corona, generated by the photospheric global oscillations the simulations use photospheric drivers mimicking the solar p -modes. The drivers are spatially structured harmonics across the computational box parallel to the solar surface. The drivers perturb the atmosphere at 0.5 Mm above the bottom boundary of the model and are placed coincident with the location of the temperature minimum. A combination of the VALIIIC and McWhirter solar atmospheres are used as the background equilibrium model.

We report how synthetic photospheric oscillations may manifest in a magnetic field free model of the quiet Sun. To carry out the simulations, we employed the magnetohydrodynamics code, SMAUG (Sheffield MHD Accelerated Using GPUs).

Our results show that the amount of energy propagating into the solar atmosphere is consistent with a model of solar global oscillations described by [Taroyan and Erdélyi \(2008\)](#) using the Klein-Gordon equation. The computed results indicate a power law which is compared to observations reported by [Ireland et al. \(2015\)](#) using data from the Solar Dynamics Observatory/Atmospheric Imaging Assembly.

Keywords: magnetohydrodynamics (MHD); oscillations; MHD waves; solar atmosphere

1. Introduction

The highly magnetised solar atmosphere exhibits a diverse range of wave phenomena. Using solar observations in the Ca K band [Leighton \(1960\)](#) reported the first observations of oscillatory behaviour with vertical motions present on the solar surface, with amplitudes of 300-400 m/s and a power peak with period of 296 s. Some years later, the detection of oscillations in the apparent solar diameter (see e.g [Hill, 1976](#); [Brown et al., 1978](#)) was one of the first suggestions of the truly global oscillations of the Sun. These ubiquitous oscillations are referred to as the solar global acoustic or p -modes. They are interpreted as trapped acoustic waves, i.e. standing acoustic oscil-

lations in the solar interior, modelled by [Ulrich \(1970\)](#). [Leibacher and Stein \(1971\)](#) reported that the vertical wavelength of these trapped oscillations is comparable to their horizontal wavelength and is around 1-5 Mm. The main restoring force for these acoustic oscillations is pressure. The solar p -modes are perturbing the photosphere. Earlier models have assumed reflection at the photosphere, and at most allowed evanescence above it. The p -modes were seen as resonant modes between the steep change in density at the solar surface and trapped beneath by the increase of the sound speed causing refraction and eventually forming a lower turning point in the interior. The observation of the resulting standing modes are now widely used as a diagnostic tool to understand the physical characteristics of the solar layers. For a review see e.g. [Christensen-Dalsgaard \(2002\)](#); [Erdélyi \(2006b,a\)](#); [Thompson \(2006\)](#); [Pintér and Erdélyi \(2011\)](#).

However, as hinted above, the global acoustic modes are not strictly trapped in the interior: either they may leak into the overlaying atmosphere or they may directly propagate into the atmosphere along magnetic field lines, especially when these magnetic waveguides are tilted away from the vertical direction, see, [De Pontieu et al. \(2003b,a, 2005\)](#). This latter realisation, if it really can happen in the Sun, may open entirely new perspectives of solar magneto-seismology (see the review by [De Pontieu and Erdélyi \(2006\)](#)).

In general, wave propagation in a medium such as the gravitationally strongly stratified solar atmosphere may be understood through the occurrence of eigen-oscillations of the medium. A model for investigating these oscillations can be tackled by studying the normal mode solutions of the gravitating hydrodynamic slab in ideal MHD, see e.g. [Goedbloed and Poedts \(2004\)](#) for an excellent mathematical and physical summary. Although the mid- to upper atmosphere is embedded in (as a first approximation highly vertical) magnetic field, as long as radial wave propagation is considered, the waves show a strong acoustic character. Therefore a hydrodynamic approximation may give a first insight in the global *atmospheric* oscillations, if any. Of course, caution has to be exercised and one must refrain from over-interpreting because the magnetic field is a key ingredient, enabling at least three types of physically distinct eigenmodes, as opposed to the single one in a hydrodynamic approximation.

Here, we report a series of hydrodynamical simulations modelling a realistic temperature, pressure and density distribution of the solar atmosphere driven by vertical velocity displacements, located at the temperature minimum mimicking the the various p -modes. The background model follows a

combination of the Vernazza et al. (1981) (VALIIIc) and McWhirter et al. (1975) model atmospheres. The driver has harmonic spatial characteristics across the base of the computational model. The objectives of this work is to model the atmospheric response generated by the global resonant acoustic oscillation at the lower boundary, in order to better understand how the energy carried by different modes of the internal acoustic oscillation are redistributed in the lower solar atmosphere and to shed light on the mechanisms which may lead to ubiquitous intensity oscillations in the solar atmosphere reported recently, see e.g. Kosovichev and Zhao (2016a), Kosovichev and Zhao (2016b), Didkovsky et al. (2013), Didkovsky et al. (2013), Ireland et al. (2015) and Erdélyi et al. (submitted 2017).

There is a significant number of works reporting on observational, theoretical and computational studies of p -mode phenomena see e.g. Christensen-Dalsgaard (2002); Erdélyi (2006b,a); Thompson (2006); Pintér and Erdélyi (2011). Observational and theoretical analysis generally describes mechanisms for the propagation of energy into the chromosphere, transition region and into the solar corona in magnetic structures (e.g. flux tubes). We briefly summarise some of the key motivations here. The growing field of solar magneto-seismology (SMS) uses the observed solar atmospheric wave modes to determine the otherwise hard to measure physical characteristics of the solar atmosphere. This, in turn, requires a thorough understanding of the physics of wave modes themselves in the solar atmosphere. Although there is overwhelming evidence for photospheric 5-minute p -modes and 3-minute chromospheric modes, the detection and characterisation of ubiquitous oscillatory phenomena in the upper atmosphere are rare and difficult to identify. This makes both the wave diagnostics and the wave heating as a possible solution to the solar atmospheric heating problem more challenging. However, since the advent of coronal seismology see e.g. (Roberts et al., 1984; Banerjee et al., 2007; De Moortel, 2005; Mathioudakis et al., 2013; Wang, 2011) many space-based high-resolution solar observations e.g. SOHO, TRACE, SDO and IRIS (to name but a few) have provided evidence for wave phenomena in the solar atmosphere.

Using SDO/AIA data we show in Figure (1) the power spectrum in nine AIA passbands for randomly selected single pixels in an Active Region (AR), Quiet Sun (QS), and a Coronal Hole (CH) on a randomly chosen day (22 August 2010) during solar minimum.

The power spectra are derived by studying image sequences at solar minimum for the different solar regions e.g. AR, a typical QS region and a CH.

The power spectra reveal strong 3-5-minute oscillations in all channels and include some longer period modes too. These results demonstrate the ubiquity of the observed 3- and 5-minute oscillations in all channels and regions and may serve as evidence of a global excitation mechanism. These observations are our strong motivation to model whether global *p*-modes may penetrate in the atmosphere.

Previously, SDO 171Å and 193Å data were also used by Ireland et al. (2015) to compute the Fourier power spectra in the solar corona. By analysing wave propagation in four regions of the solar atmosphere with different characteristics, they found that the distribution obeys a power law at low frequencies and possesses a flat distribution at high frequencies. This contrasts with the idea of a Gaussian noise distribution and a long time-scale background. The implication is that this is the result of solar atmospheric energy propagation from elsewhere by small energy deposition events.

Evidence for the upward propagation of acoustic waves with increasing amplitude has been demonstrated through studies of variation in the intensities of chromospheric lines, for example the Ca lines at 854 nm, see Beck et al. (2012). Although the observed variations are unlikely to provide temperature rises well-known in the chromosphere they are a clear indication of the increase in dynamical activity from the photosphere to the chromosphere. The analysis of observations by Bello González et al. (2009) finds that at a height of 250 km there is an acoustic energy flux of 3000 W/m^2 , 2/3 of this energy is propagated by waves in the frequency range 5-10 mHz, the remaining third is carried by waves in the frequency range 10-20 mHz. Waves with frequencies greater than the acoustic cut-off of 190 s can contribute to the heating of the solar chromosphere. Reporting on measurements from the Fe I 5434, Å Bello González et al. (2010) detected waves with periods down to 40 s. For periods below the cut-off of 190 s 40% of wave detections are above granules the remaining 60% are above the intergranules. The reported best estimate of the energy flux above granules is around 3000 W/m^2 whilst above the intergranules it is around 955 W/m^2 . Most of the acoustic flux is found between 110 s and 193 s.

Using the IMAX instrument on the Sunrise observatory, Roth et al. (2010) reported evidence for the excitation of solar acoustic oscillations excited by turbulent flows in the dark intergranular lanes. Individual sunquakes with epicentres near the solar surface and located in the intergranular lanes, are assumed to feed continuously energy into the resonant *p*-modes of the Sun and provide sources for acoustic oscillations. Roth et al. (2010) presents

wavefronts rippling near a granule and oriented along the direction of the intergranular lane. Using simultaneous observations of the Na and K lines with Doppler measurements, [Jefferies et al. \(2006\)](#) shows that inclined magnetic field lines provide portals along which magneto-acoustic energy can propagate at the intergranular boundaries.

There is a large body of computational work already undertaken to understand the propagation of waves in the solar atmosphere. Previous work, e.g. [Erdélyi et al. \(2007\)](#), has considered point source drivers with a gaussian velocity distribution. Later, [Fedun et al. \(2009\)](#) studied the oscillatory response of the 3D solar atmosphere to the leakage of photospheric motion results are discussed in detail. High-frequency waves are shown to propagate from the lower atmosphere across the transition region, experiencing relatively low reflection, and transmitting most of their energy into the corona. It is also observed that the thin transition region becomes a wave guide for horizontally propagating surface waves for a wide range of driver periods, particularly at those periods that support chromospheric standing waves. Additionally, the magnetic field acts as a waveguide for both high- and low-frequency waves originating from the photosphere and propagating through the transition region into the solar corona. Other work, e.g. [Murawski and Zaqrashvili \(2010\)](#), has demonstrated that a strong initial pulse may lead to the quasi periodic rising of chromospheric material into the lower corona in the form of spicules, see also e.g. [Khomenko and Calvo Santamaria \(2013\)](#). [Kalkofen et al. \(2010\)](#), considered the propagation of acoustic modes in a stratified hydrodynamical model of the solar atmosphere with a cylindrically symmetric driver of diameter 1Mm, they conclude that for driving regions of sizes smaller than the atmospheric scale height they are able to reproduce expansion waves which are similar to chromospheric bright points. With a weak horizontal magnetic field, the physics within the interior of supergranulation cells [Lites et al. \(2008\)](#) is suitably simple for undertaking hydrodynamic modelling. The modes modelled in this paper are mimicking global eigenmodes, the coherence length of eigenoscillations at the photosphere is 4 Mm, and the power peaks at 5 mins.

2. Numerical Computation Methods

The 3D numerical simulations described here were undertaken using Sheffield MHD Accelerated Using GPUs (SMAUG, [Griffiths et al., 2015](#)), the GPU implementation of the Sheffield Advanced Code (SAC, [Shelyag et al., 2008](#)).

SAC and SMAUG are numerical MHD solvers allowing us to model the time-dependent evolution of photospheric oscillations in the solar atmosphere. SAC is a derivative of the versatile advection code (VAC) developed by (Tóth, 1996). The general system of ideal MHD equations are

$$\frac{\partial \rho}{\partial t} + \nabla \cdot (\rho \mathbf{v}) = 0, \quad (1)$$

$$\frac{\partial(\rho \mathbf{v})}{\partial t} + \nabla \cdot (\mathbf{v} \rho \mathbf{v} - \mathbf{B} \mathbf{B}) + \nabla p_t = \rho \mathbf{g}, \quad (2)$$

$$\frac{\partial e}{\partial t} + \nabla \cdot (\mathbf{v} e - \mathbf{B} \mathbf{B} \cdot \mathbf{v} + \mathbf{v} p_t) + \nabla p_t = \rho \mathbf{g} \cdot \mathbf{v}, \quad (3)$$

$$\frac{\partial \mathbf{B}}{\partial t} + \nabla \cdot (\mathbf{v} \mathbf{B} - \mathbf{B} \mathbf{v}) = 0. \quad (4)$$

Here, ρ is the mass density, \mathbf{v} is the velocity, \mathbf{B} is the magnetic field, e is the energy density, p_t is the total pressure and \mathbf{g} is the gravitational acceleration vector. The total pressure p_t is written as

$$p_t = p_k + \frac{\mathbf{B}^2}{2}, \quad (5)$$

where p_k is the kinetic pressure given by

$$p_k = (\gamma - 1) \left(e - \frac{\rho \mathbf{v}^2}{2} - \frac{\mathbf{B}^2}{2} \right). \quad (6)$$

Equations (1) - (6) are applicable to an ideal compressible plasma. The SAC code is based on perturbed versions of these equations, thus the variables ρ , e and \mathbf{B} are expressed in terms of perturbed and background quantities as

$$\begin{aligned} \rho &= \tilde{\rho} + \rho_b, \\ e &= \tilde{e} + e_b, \\ \mathbf{B} &= \tilde{\mathbf{B}} + \mathbf{B}_b. \end{aligned}$$

where $\tilde{\rho}$ is the perturbed density, \tilde{e} is the perturbed energy and $\tilde{\mathbf{B}}$ is the perturbed magnetic field. The background quantities with a subscript b do not change in time, as we assume a magneto-hydrostatic equilibrium of the background plasma.

The SMAUG code is a fully non-linear MHD numerical finite element solver for simulating, linear and non-linear wave propagation in strongly magnetised plasma with structuring and stratification. The solver applies a fourth

order central differencing technique to the spatial derivatives and the Euler or fourth order Runge-Kutta method to solve the temporal derivatives. By virtue of their symmetry, central differencing schemes are conservative, with the desired side effect that the solver conserves the divergence of the magnetic field. The application of central differencing to hyperbolic differential equations results in unstable solutions with a spurious oscillatory behaviour. Hyper-diffusion and hyper-resistivity are implemented to achieve numerical stability of the computed solution of the MHD equations (see for example [Caunt and Korpi, 2001](#)). The primary purpose of the diffusion terms is to compensate for the anti-diffusion from truncation errors arising in the computation of temporal and spatial derivatives. When the diffusion is correctly tuned the resulting evolution is non-diffusive. In addition, the diffusion terms control the steepness of shocks by becoming large wherever the compression is large. The full set of MHD equations, including the hyper-diffusion source terms are given in [Griffiths et al. \(2015\)](#) and [Shelyag et al. \(2008\)](#).

3. Computational Model

With the magnetic-field-free quiet Sun in mind, we set $\vec{B} = 0$ in the MHD equations. The computational box used for our simulations represents a volume of the solar atmosphere with dimensions $L_x = 4$ Mm and $L_y = 4$ Mm. The model utilises a representation of the solar atmosphere with gravitational stratification in the z -direction and with a height of $L_z = 6$ Mm. The computational box comprises an array of elements of dimension $128 \times 128 \times 128$. The upper boundary of our model is in the solar corona and the lower boundary in the photosphere. The SMAUG code is well suited for modelling the leakage of wave energy from the photosphere, through the transition region and into the corona. We used open boundary conditions for all of the boundaries, this allowed us to model wave propagation for time scales characterised by the 5-minute p -mode induced oscillations. The computational model is excited by an extended vertical velocity driver located at the photosphere, this acoustic p -mode driver excites waves which propagate into a realistic 3D model of the solar atmosphere. In the following two sections we describe the solar atmospheric model and the implementation of the driver.

4. Solar Atmospheric Model

To simulate oscillatory phenomena in the solar corona a physically representative model of the solar atmosphere is needed. An option is the use of

a parametrisation of the temperature of the solar atmosphere which may be a smoothed step function profile see [Murawski and Zaqrashvili \(2010\)](#). Results have demonstrated the need for observationally derived semi-empirical models of the solar atmosphere. There is much discussion about model validity and the work undertaken to demonstrate the reliability of the assumptions used to construct realistic models of the solar chromosphere, see [Carlsson and Stein \(1995\)](#), [Kalkofen \(2012\)](#). The contention arises from the dynamical nature of the solar chromosphere; for example local dynamo action has been suggested as a mechanism of Joule heating in the solar chromosphere, see [Leenaarts et al. \(2011\)](#). The model atmosphere employed here is an observationally derived semi-empirical representation of the quiet sun. With the fundamental assumption of hydrostatic equilibrium a model of the chromosphere in equilibrium is constructed using the VALIIIc model, see [Vernazza et al. \(1981\)](#). For the region of the solar atmosphere above 2.5 Mm the results of the energy balance model of solar coronal heating has been used (see [McWhirter et al., 1975](#)), his model includes an acoustic contribution comparable to the hydrostatic pressure. The corresponding temperature and density profiles are shown in Figure (2).

5. Numerical Drivers for p -mode Oscillations

For this study, the model requires a driver mimicing the solar global oscillations. The overview of observational studies identified a range of physical phenomena resulting in oscillatory behaviour and delivering energy into the solar atmosphere. The results presented here extend earlier work undertaken by [Malins \(2007\)](#), for their study, point drivers were used to represent periodic buffeting of turbulent motions in the photosphere. The results of the study demonstrated surface wave phenomena and structures in the transition region. The study highlighted the characteristics of the oscillatory phenomena as a result of frequency cut-offs induced by the stratified solar atmosphere. In contrast to the earlier models, for the simulations presented in this paper, the whole boundary of the model was perturbed. In the real Sun, photospheric p -mode oscillations have a horizontal wavelength and coherence. Here, these excitations are represented with a vertical velocity driver located at the photosphere, this acoustic p -mode driver excites waves which propagate into a realistic 3D model of the solar atmosphere. Drivers representing different modes are considered, for example an extended driver with a sinusoidal dependence and a wavelength of 8 Mm applied along the middle of the base of

a computational domain of dimension 4 Mm represents a *fundamental mode*. A driver with wavelength 4 Mm applied the same way represents the *first harmonic* and *second harmonic* with wavelength 2 Mm was also considered. Drivers may be constructed as an ensemble of these solar global eigenmodes. Such a driver may be represented by the expression shown in equation (7)

$$V_z = A_{nm} \sin\left(\frac{2\pi t}{T_s}\right) \sin\left(\frac{(n+1)\pi x}{L_x}\right) \sin\left(\frac{(m+1)\pi y}{L_y}\right) \exp\left(-\frac{(z-z_0)^2}{\Delta z^2}\right), \quad (7)$$

In equation (7) L_x and L_y are the lengths of the base of the simulation box in the x and y directions respectively. T_s is the period and A_{nm} is the amplitude of the driver, the indices n and m define the mode. Δz is the width of the driver which was set here to 4 km, the parameter z_0 was set so that the vertical driver location is coincident with the location of the temperature minimum which is 0.5 Mm above the lower boundary of the model i.e. the photosphere. Since we are investigating the leakage of energy into the solar atmosphere, for consistency, it is necessary to ensure that for the different modes the driver amplitude is set to a value which provides the same total amount of energy over the model cross section and per unit time. For the n, m mode the energy, E_{nm} as a function of z and time may be written as;

$$E_{nm}(z, t) = \rho A_{nm}^2 I_{nm} \sin\left(\frac{2\pi t}{T_s}\right)^2 \exp\left(-\frac{(z-z_0)^2}{\Delta z^2}\right)^2, \quad (8)$$

where I_{nm} is

$$I_{nm} = \int_{-L_x}^{L_x} \int_{L_y}^{+L_y} \sin\left(\frac{(n+1)\pi x}{L_x}\right)^2 \sin\left(\frac{(m+1)\pi y}{L_y}\right)^2 dx dy.$$

It is necessary to determine the amplitude A_{nm} for the different modes n, m with driver period T_s . This is achieved by computing the membrane energy, E_{nm} , integrated over the surface area and over a period of time from $t = 0$ to $t = T_m$ where T_m will correspond to the period of the driver with the largest value for the period. Following Leighton (1960), for the fundamental mode with driver period 300 s, we set $A_{00}=350 \text{ ms}^{-1}$. Using Equation (8) to derive the ratio of the membrane energy for the mode n, m with driver period T_s , the mode $(0, 0)$ with driver period T_{00} and making $L_x = L_y$ gives the relation

$$A_{nm}^2 = \frac{2A_{00}^2}{(n^2 + m^2 + 2(n+m) + 2)} T_{rat}, \quad (9)$$

Set	Description
A	Modes for the 30, 180 and 300 s driver.
B	Normal Modes corresponding to different values of c_s
C	Normal Modes for equal mode values (i.e. $n = m$)

Table 1: Sets of simulations used to characterise oscillatory motions arising from an extended photospheric driver.

where T_{rat} is

$$T_{rat} = \frac{T_m - \frac{T_{00}}{4\pi} \sin(\frac{4\pi T_m}{T_{00}})}{T_m - \frac{T_s}{4\pi} \sin(\frac{4\pi T_m}{T_s})}.$$

This relation was used to determine the amplitudes for the higher order modes, starting from the A_{00} mode, with, $A_{00} = 350 \text{ ms}^{-1}$.

6. Numerical Analysis

Hydrodynamic simulations have been undertaken for a selection of drivers covering a range of time periods, modes and amplitudes supplying the same amount of energy. For this investigation we have been guided by the requirement that different driver modes deliver the same total amount of energy over the model cross section and when integrated over a time interval corresponding to the period of the longest period driver used for the set of simulations. With the objective to analyse and understand the nature of the energy propagation of the different modes and driver frequencies we consider a number of cases. Three sets of simulations have been considered. Set (A) are the drivers selected because of their period. Set (B) and (C) are series of normal modes, set (C) are normal modes with equal mode numbers (see Table (1)). The driver periods for set (A) correspond to the dominant atmospheric modes of oscillation, for example, the 5-minute mode and the 3-minute chromospheric mode. The 30 s driver was selected because this corresponds to a frequency below that of the atmospheric cut-off and we can use the propagation characteristics as a test of our simulations. The driver periods for the normal modes are determined using the mode numbers, a value for the speed of sound (see table (2)) and equation (11). The amplitudes for each of the modes are determined by using Equation (9). The periods for the normal modes were determined for different values of the speed of sound (c_s) in the solar atmosphere at different heights. The computed periods for the

Mode	20 km/s	31.4 km/s
0,0	282.8	180.0
0,1	200.0	127.3
0,2	133.3	84.8
0,3	100.0	63.6

Table 2: The table shows the driver periods used for different wave modes. The first mode number corresponds to the mode for the x -direction and the second number the mode for the y -direction. The table corresponds to the normal modes labelled set B. The table column headings show the value of the speed of sound, c_s , which was used to compute the frequency of the normal mode using equation 11.

Mode	Period (s)
1,1	471.4
2,2	235.7
3,3	157.1

Table 3: The table shows the driver periods used for different wave modes. The first mode number corresponds to the mode for the x -direction and the second number the mode for the y -direction. The table corresponds to the normal modes labelled set C. The table column headings show the value of the speed of sound, c_s , which was used to compute the frequency of the normal mode using equation 11.

resulting drivers with different mode numbers are shown in Tables (2) , (3). Table (4) shows the amplitudes for the drivers from set (A).

$$\omega_{nm}^2 = k_{nm}^2 c_s^2, \quad (10)$$

where c_s is the speed of sound in the solar atmosphere and k_{nm} is the wave number for the mode determined using the number of wavelengths accomodated within the fixed simulation box length.

7. Results of Numerical Simulation

The propagation of waves in a stratified atmosphere can be understood using linearised versions of the equation of continuity, momentum and energy. Such atmospheric waves of expansion have been considered for many years, initiated by e.g. Lamb (1932). Owing to the high gradients, partial reflection of acoustic waves at all frequencies is expected at the transition region. The transition region is the upper boundary of the chromospheric cavity, it has been previously suggested that this is the source of three-minute

Mode	30 s driver	180 s s driver	300 s s driver
0,0	343.4	348.3	350.0
0,1	217.2	220.3	221.4
0,2	153.6	155.8	156.5
0,3	117.8	119.5	120.0

Table 4: The table shows the driver amplitudes used for different wave modes. The first mode number corresponds to the mode for the x -direction and the second number the mode for the y -direction. The table corresponds to the modes labelled set A. The table column headings show the driver period each table entry shows the amplitude computed using equation 9.

	1 Mm	2 Mm	4 Mm	5.5 Mm
30	0.0133	1.7275x10 ⁻⁴	1.0561x10 ⁻⁴	5.5399x10 ⁻⁵
300	0.2607	0.008144	0.002176	0.001119
180	0.7227	0.047895	0.019831	0.010365
435.1	1.9415	0.043601	0.005944	0.003147
179.98	1.6450	0.004502	0.002600	0.001366

Table 5: (0, 0) mode energy ratio, the energy is the ratio of the energy flux at a given height to the energy flux at the location of the driver. The height at which the energy flux ratio is computed is shown in the column heading.

transition-region oscillations, see [Leibacher and Stein \(1971\)](#). It is known that the propagation of acoustic waves in an unbounded stratified medium is determined by a cut-off period. In a gravitationally stratified atmosphere acoustic waves can only propagate if the wave period is less than the cut-off period. Waves with a period greater than the cut-off are evanescent. Following [Taroyan and Erdélyi \(2008\)](#), by solving the Klein-Gordon equation for the gravitationally stratified atmosphere i.e,

$$\frac{\partial^2 Q}{\partial t^2} - c_s^2(z) \frac{\partial^2 Q}{\partial z^2} + \Omega^2(z)Q = 0,$$

The quantity $\Omega(z)$ represents the acoustic cut-off frequency. The cut-off period, $P_c(z)$, for the atmosphere at a given height, z , can be obtained from:

$$P_c(z) = \frac{2\Lambda_0}{c_s(z)} \sqrt{\frac{1}{1 + 2\frac{d}{dz}\Lambda_0(z)}}.$$

	1 Mm	2 Mm	4 Mm	5.5 Mm
30	0.0065	1.751x10 ⁻⁵	1.2579x10 ⁻⁶	4.6820x10 ⁻⁷
300	0.1001	8.796x10 ⁻⁴	4.1494x10 ⁻⁶	1.3059x10 ⁻⁶
180	0.1543	5.8381x10 ⁻⁴	3.2715x10 ⁻⁵	1.1343 x10 ⁻⁵
307.1	0.0982	0.001	4.1351x10 ⁻⁶	1.3380 x10 ⁻⁶
127.27	0.0829	4.3190x10 ⁻⁴	5.1387x10 ⁻⁵	2.0397 x10 ⁻⁵
200.0	0.1126	4.4180x10 ⁻⁴	2.0186x10 ⁻⁵	6.3062 x10 ⁻⁶

Table 6: (0, 1) mode energy ratio, the energy is the ratio of the energy flux at a given height to the energy flux at the location of the driver. The height at which the energy flux ratio is computed is shown in the column heading.

	1 Mm	2 Mm	4 Mm	5.5 Mm
30	0.0024	7.2158 x10 ⁻⁶	1.0651x10 ⁻⁶	7.6079x10 ⁻⁷
300	0.0578	4.9604 x10 ⁻⁴	5.5618x10 ⁻⁶	4.1907x10 ⁻⁶
180	0.0687	3.5547 x10 ⁻⁴	6.0675x10 ⁻⁵	4.1492 x10 ⁻⁵
205.1	0.3135	0.0015	1.6520x10 ⁻⁴	1.1272x10 ⁻⁴
84.84	0.0206	5.8903 x10 ⁻⁵ 1.6520 x10 ⁻⁵	1.1890 x10 ⁻⁵	
133.33	0.0497	1.9731x10 ⁻⁴ 7.9834 x10 ⁻⁵	5.6267 x10 ⁻⁵	

Table 7: (0, 2) mode energy ratio, the energy is the ratio of the energy flux at a given height to the energy flux at the location of the driver. The height at which the energy flux ratio is computed is shown in the column heading.

Where the pressure scale height for an atmosphere stratified by a uniform gravitational field is given by

$$\Lambda_0(z) = \frac{p_0(z)}{g\rho_0(z)}.$$

Here, $p_0(z)$ and $\rho_0(z)$ are the equilibrium pressure and density as a functions of height, respectively. Q is the re-scaled perturbation of the velocity. The variation of the cut-off frequency, $\Omega(z)$, as a function of solar atmospheric height is shown in Figure (2) (see upper panel) which unveils the cut-off period for the case of VALIII atmosphere and isothermal atmosphere, respectively. It is recognised from Figure (2) that there are a number of distinct regions of propagation behaviour. For the photosphere, near the temperature minimum, the cut-off period is 300 s, therefore, it is expected that the 5 minutes modes are evanescent. In the chromosphere the cut-off period increases to a value greater than 300 s, therefore the five minute modes

	1 Mm	2 Mm	4 Mm	5.5 Mm
30	0.0101	4.2736x10 ⁻⁵	6.3291x10 ⁻⁷	3.7786x10 ⁻⁷
300	0.0359	3.8929x10 ⁻⁴	3.2621x10 ⁻⁷	2.1259x10 ⁻⁷
180	0.0351	1.3948x10 ⁻⁴	3.1342x10 ⁻⁶	1.8205x10 ⁻⁶
153.8	0.0313	1.1043x10 ⁻⁴	3.8071x10 ⁻⁶	2.1034x10 ⁻⁶
63.63	0.0051	9.8989x10 ⁻⁶	7.0207x10 ⁻⁷	4.0621x10 ⁻⁷
100.0	0.0151	3.0678x10 ⁻⁵	2.8527x10 ⁻⁶	1.6707x10 ⁻⁶

Table 8: (0,3) mode energy ratio, the energy is the ratio of the energy flux at a given height to the energy flux at the location of the driver. The height at which the energy flux ratio is computed is shown in the column heading.

	1 Mm	2 Mm	4 Mm	5.5 Mm
(0, 0)	0.7227	0.0479	0.0198	0.0104
(0, 1)	0.1543	0.0006	3.2715x10 ⁻⁵	1.1343x10 ⁻⁵
(0, 2)	0.0687	0.0004	6.0675x10 ⁻⁵	4.1492x10 ⁻⁵
(0, 3)	0.0351	0.0001	3.1342x10 ⁻⁶	1.8205 x10 ⁻⁶
(1, 1)	0.4072	0.0011	4.5311x10 ⁻⁶	5.5495x10 ⁻⁷
(1, 2)	0.3331	0.0012	3.0728x10 ⁻⁶	1.3055x10 ⁻⁶
(1, 3)	0.2961	0.0011	4.8733x10 ⁻⁷	3.4760x10 ⁻⁷
(2, 2)	0.3054	0.0011	1.5844x10 ⁻⁵	1.7622x10 ⁻⁵
(2, 3)	0.2732	0.0008	2.1443x10 ⁻⁶	1.7045x10 ⁻⁶
(3, 3)	0.2205	0.0006	1.9711x10 ⁻⁷	2.6756x10 ⁻⁷

Table 9: 180 s driver energy ratio, the energy is the ratio of the energy flux at a given height to the energy flux at the location of the driver. The height at which the energy flux ratio is computed is shown in the column heading.

can propagate once they are either excited here or can propagate here due to e.g. leakage. For the transition zone the cut-off drops to a value which goes down to 100 s. In the corona, it is seen that a much greater range of frequencies can propagate.

To determine how wave energy propagation is influenced by the wave modes and frequencies, we compute the time averaged wave energy flux integrated over the cross-sectional area of the simulation box at different heights. The area of integration is perpendicular to the model z -axis.

$$F_{int} = \frac{1}{t_{max}} \int_0^{t_{max}} \int \mathbf{F}_{wave} \cdot d\mathbf{A} dt, \quad (11)$$

	1 Mm	2 Mm	4 Mm	5.5 Mm
(0, 0)	0.2607	0.0081	2.2x10 ⁻³	1.1x10 ⁻³
(0, 1)	0.1001	0.0009	4.1494x10 ⁻⁶	1.3059x10 ⁻⁶
(0, 2)	0.0578	0.0005	5.5618x10 ⁻⁶	4.1907x10 ⁻⁶
(0, 3)	0.0359	0.0004	3.2621x10 ⁻⁷	2.1259x10 ⁻⁷
(1, 1)	0.2267	0.0016	9.9329x10 ⁻⁷	1.0749x10 ⁻⁷
(1, 2)	0.2535	0.0016	8.2058x10 ⁻⁷	2.8814x10 ⁻⁷
(1, 3)	0.2692	0.0023	2.1995x10 ⁻⁷	9.0161x10 ⁻⁸
(2, 2)	0.2625	0.0021	1.4846x10 ⁻⁶	1.7399x10 ⁻⁶
(2, 3)	0.2328	0.0017	2.4839x10 ⁻⁷	2.0699x10 ⁻⁷
(3, 3)	0.2036	0.0012	7.2069x10 ⁻⁸	4.944x10 ⁻⁸

Table 10: 300 s driver energy ratio, the energy is the ratio of the energy flux at a given height to the energy flux at the location of the driver. The height at which the energy flux ratio is computed is shown in the column heading.

where the wave energy flux \mathbf{F}_{wave} is given by

$$\mathbf{F}_{\text{wave}} = \tilde{p}_k \mathbf{v}.$$

The expression for the wave energy flux is dependent on the perturbed kinetic pressure, \tilde{p}_k , given by [Bogdan et al. \(2003\)](#)

$$\tilde{p}_k = (\gamma - 1) \left(\tilde{e} - \frac{(\tilde{\rho} + \rho_b) \mathbf{v}^2}{2} \right).$$

The full set of videos for all the simulations performed have been made publically available on the digital media repository hosted by The University of Sheffield, see [Griffiths et al. \(2017\)](#). Each video shows the value of the vertical component of the plasma velocity (z -component) along different slices through the simulation box. The scale shows the velocity in m/s. The green vectors represent the velocity directions along a single slice through the simulation. The green surface at a height of 3.5 Mm is the 2 MK temperature isosurface. Each video is labelled using three numbers. The first number is the driver period in seconds. The following 2 integers are each of the mode indices for the x - and y -direction, respectively.

For the fundamental modes (0, 0) with the 30, 180 and 300 s drivers we have produced time-distance plots of the plasma velocity, v_z , i.e., in the same direction as the driver and in the direction of increasing height through

the solar atmosphere. The fundamental modes illustrated in Figures (3-6) demonstrate that there is no significant structure at the transition zone. However, the 30 s mode demonstrates the rapid expansion of the perturbation at the penetration height of the the transition region. This is accompanied with an increase in the transverse velocity (v_x). This observation is true for all 30, 180 and 300 s driver scenarios. As the mode order is increased from $n = 0$, to $n = 1$ and then $n = 2$ it is observed that transition region structuring becomes apparent and is more reminiscent of the observations of [Malins \(2007\)](#).

Figure (7) shows the time-distance plots for a vertical section through the simulation box, since this was a fundamental mode the section was taken through the middle of the simulation box. The plots show that the greatest amplitude arises in the transition region. Looking at the result for the 30 s driver, it is seen that the initial travelling response reaches a response at around 0.5 Mm corresponding to a cut-off of 200 s. The maximum amplitude is coherent with the maximum occurring at the same frequency as that of the driver. For the first 70 periods, maxima appear in the transition zone. It also appears that the transition zone is essentially a source of excitation with frequency lower than that of the driver, however, at longer time periods these motions occur with reduced amplitude but with the same period as the driver. For the 180 and 300 s drivers it is observed that the amplitude in the transition zone is larger than that for the 30 s driver by a factor of up to 20. For the 30, 180 and 300 s cases we observe the travelling wave in the chromosphere and in the solar corona. Although the 180 s mode shows the greatest excitation, both the 180 and 300 s drivers become evanescent due to the cut-off period for the upper atmosphere. The intensity peak for the 180s driver is a result of the Chromospheric resonance which is well documented, see for example [Fleck and Schmitz \(1991\)](#).

The time-distance plots for horizontal sections are illustrated in Figures (8-13), at an atmospheric height of 4.2 Mm there is a clear indication of the propagation of waves across the transition zone. For the 30 s driver it can be seen that the propagation is cut-off after the first 270 s of the simulation. All three driver cases indicate a peak with a width of around 90 s. This peak exhibits a degree of splitting which is most clear for the 300 s driver. This effect may be attributable to the superposition of waves reflected from the boundaries of the chromosphere. Figures 8 and 11 show the time-distance plots for a horizontal section taken at a height of 0.94 Mm, i.e. through the chromosphere. The travelling modes in these plots propagate as plane modes

Ireland (193Å)	((00) mode at 5.5Mm)	((00) mode at 2Mm)	Ireland (171Å)
a $10^{-0.1}$	-0.000805	-0.003733	$10^{0.57}$
b 2.2	2.732	2.716	1.72
c $10^{-3.52}$	1.096×10^4	4.724×10^4	10^{-3}

Table 11: Power law coefficients for relationship between power and time-period of atmospheric oscillation.

with a frequency consistent with that of the driver. The greatest intensity is observed for the 180 s driver. Propagation for the transition zone shows the most powerful response for the 180 s driver followed by the 300 s driver. The response for the 30 s driver decays rapidly after the first ten cycles. As we move into the solar corona there is further attenuation with the greatest signal reduction for the 30 s driver.

Using equation (11), we computed the energy flux integral for each of the drivers at different atmospheric heights. Figure 18 and figure 15 show plots of the computed energy flux ratios for two sets of simulations. In the first case we show the energy flux ratios for our drivers each delivering the same amount of energy, in the second case (figure 17), we plot the energy ratios for another set of simulations but where we kept the driver amplitude fixed at the same amplitude for all mode numbers and driver frequencies. The energy flux ratio is the ratio of the energy flux at a given height to the energy flux at the location of the driver.

The tables 5,6,7 and 8 show the resulting values of the energy flux ratio from the simulations at different heights. All the modes for the driver periods of 180 s and 300 s are shown as a bar chart in figures (16) and (17), see also tables 9 and 10. For both the 180 s and 300 s drivers it can be seen that the even modes make the strongest contribution in the corona. The results plotted in figure (18) show the ratio of the energy flux for models delivering the same quantity of energy to the energy flux for models where the driver amplitude is kept fixed. With the exception of the fundamental mode, the ratios appear to be constant for all frequencies suggesting the possibility of using the scaling relation to compute the energy flux for different frequencies and modes.

Fitting the data for the $(0, 0)$ mode against the power law shown in equation (12) gives the values shown in Table 11, we obtain power laws for the energy flux at $5.5Mm$ and the energy flux at $2Mm$. Figure 18 shows a comparison of the energy flux ratio for the $(0, 0)$ -mode with the observational power law ratio from the results of Ireland et al. (2015). For the simulation results we compute the ratio of the energy flux at $5.5Mm$ to the energy flux at $2Mm$. For the observational data we compute the ratio of the power laws for the results at 171\AA and the results at 193\AA . Six pairs of period and flux values were used for the fitting procedure. The results suggest that our simulated data give rise to a flat power spectrum as opposed to the power law suggested by Ireland et al. (2015).

$$P(z) = aT^b + c, \quad (12)$$

8. Conclusions

In this paper, motivated by the reported plentiful intensity oscillations at various layers of the solar atmosphere from low chromosphere to corona detected by the currently available suite of high-resolution space-based instrumentation (e.g. SDO), we embarked on a simple model to investigate whether these oscillations may be linked to the global solar acoustic oscillations of the photosphere. We approximated the solar atmosphere by a purely hydrodynamic VAL III-type of equilibrium. The perturbations mimicking the photospheric coherence pattern of a range of periods of p -mode oscillations were implemented at the lower boundary of the simulation box. The perturbations themselves were only allowed in the vertical (i.e. radial) direction. Therefore waves were propagating along the z -axis from the photosphere into the lower solar corona.

Our results support the notion that solar global oscillations may be a driver for a range of global dynamical phenomena resulting in chromospheric and low coronal Doppler and intensity oscillations which, after all, may contribute to the non-thermal energy present in the solar atmosphere. We would like to emphasise that these upper atmospheric ubiquitous wave phenomena may not arise solely from the photospheric p -modes. On the contrary, a range of sources including, turbulent motions from convective cells, local nano-flares, small-scale Kelvin-Helmholtz instabilities, or continuous reconnection events in the magnetic carpet may contribute to their excitation.

Among others, we found that

1. there is consistency between the frequency-dependence of the energy flux in the numerical simulations and power flux measurements obtained from SDO;
2. energy propagation into the mid- to upper-atmosphere of the quiet Sun occurs for a range of frequencies and may explain observed intensity oscillations for periods greater than the well known 3-minute and 5-minute oscillations;
3. energy flux propagation into the lower solar corona is strongly dependent on the particular wave modes;
4. agreement between the energy flux predictions of our numerical simulations and that of the two layer Klein-Gordon model supports our interpretation of the interaction of solar global oscillations with the solar atmosphere.

An important caveat of the present work is the modelling of the active response of the atmospheric magnetic field. Although the plasma- β may be very low in the low corona, this approximation may serve an appropriate initial insight, nevertheless one needs to relax this condition and analyse how perhaps the mean magnetic field itself would change the coupling of the global solar acoustic modes to the overlaying magnetised atmosphere. Here, an interesting question would be to investigate whether slow or fast MHD waves are the key stakeholders in the re-distribution of the convective kinetic energy.

9. Acknowledgements

The authors thank P. H. Keys for providing the wavelet tools to analyse the related SDO data, and, the Science and Technology Facilities Council (STFC), UK for the support they received. VF thanks the Royal Society-Newton Mobility Grant and Newton Fund MAS/CONACyT Mobility Grants Program for the support received. RE acknowledges the support received from the the Royal Society (UK). We acknowledge Corporate Information and Computing Services at The University of Sheffield for the provision of the High Performance Computing Service.

References

Banerjee, D., Erdélyi, R., Oliver, R., O’Shea, E., 2007. Present and Future Observing Trends in Atmospheric Magnetoseismology. Sol. Phys.246, 3–29.

- Beck, C., Rezaei, R., Puschmann, K. G., 2012. The energy of waves in the photosphere and lower chromosphere. II. Intensity statistics. *A&A*544, A46.
- Bello González, N., Flores Soriano, M., Kneer, F., Okunev, O., 2009. Acoustic waves in the solar atmosphere at high spatial resolution. *A&A*508, 941–950.
- Bello González, N., Flores Soriano, M., Kneer, F., Okunev, O., Shchukina, N., 2010. Acoustic waves in the solar atmosphere at high spatial resolution. II. Measurement in the Fe I 5434 Å line. *A&A*522, A31.
- Bogdan, T. J., Carlsson, M., Hansteen, V. H., McMurry, A., Rosenthal, C. S., Johnson, M., Petty-Powell, S., Zita, E. J., Stein, R. F., McIntosh, S. W., Nordlund, Å., 2003. Waves in the Magnetized Solar Atmosphere. II. Waves from Localized Sources in Magnetic Flux Concentrations. *ApJ*599, 626–660.
- Brown, T. M., Stebbins, R. T., Hill, H. A., 1978. Long-period oscillations of the apparent solar diameter - Observations. *ApJ*223, 324–338.
- Carlsson, M., Stein, R. F., 1995. Does a nonmagnetic solar chromosphere exist? *ApJL*440, L29–L32.
- Caunt, S. E., Korpi, M. J., Apr. 2001. A 3D MHD model of astrophysical flows: Algorithms, tests and parallelisation. *A&A*369, 706–728.
- Christensen-Dalsgaard, J., 2002. Helioseismology. *Reviews of Modern Physics* 74, 1073–1129.
- De Moortel, I., 2005. An overview of coronal seismology. *Philosophical Transactions of the Royal Society of London Series A* 363, 2743–2760.
- De Pontieu, B., Erdélyi, R., 2006. The nature of moss and lower atmospheric seismology. *Philosophical Transactions of the Royal Society of London Series A* 364, 383–394.
- De Pontieu, B., Erdélyi, R., De Moortel, I., 2005. How to Channel Photospheric Oscillations into the Corona. *ApJL*624, L61–L64.
- De Pontieu, B., Erdélyi, R., de Wijn, A. G., 2003a. Intensity Oscillations in the Upper Transition Region above Active Region Plage. *ApJL*595, L63–L66.

- De Pontieu, B., Tarbell, T., Erdélyi, R., 2003b. Correlations on Arcsecond Scales between Chromospheric and Transition Region Emission in Active Regions. *ApJ*590, 502–518.
- Didkovsky, L., Kosovichev, A., Judge, D., Wieman, S., Woods, T., 2013. Variability of Solar Five-Minute Oscillations in the Corona as Observed by the Extreme Ultraviolet Spectrophotometer (ESP) on the Solar Dynamics Observatory/Extreme Ultraviolet Variability Experiment (SDO/EVE). *Sol. Phys.*287, 171–184.
- Erdélyi, R., 2006a. Magnetic coupling of waves and oscillations in the lower solar atmosphere: can the tail wag the dog? *Philosophical Transactions of the Royal Society of London Series A* 364, 351–381.
- Erdélyi, R., 2006b. Magnetic seismology of the lower solar atmosphere. In: Proceedings of SOHO 18/GONG 2006/HELAS I, Beyond the spherical Sun. Vol. 624 of ESA Special Publication. p. 15.1.
- Erdélyi, R., Fedun, V., Malins, C., Pintér, B., 2007. Trapped Eigenoscillations in the Lower Solar Atmosphere: Is there a Resonant Coupling? In: Heinzel, P., Dorotovič, I., Rutten, R. J. (Eds.), *The Physics of Chromospheric Plasmas*. Vol. 368 of Astronomical Society of the Pacific Conference Series. pp. 187–192.
- Erdélyi, R., Zheng, R., Verth, G., Keys, P., submitted 2017. Ubiquitous concurrent intensity oscillations in the solar atmosphere detected by SDO/AIA. *ApJ*, 25 pages.
- Fedun, V., Erdélyi, R., Shelyag, S., Sep. 2009. Oscillatory Response of the 3D Solar Atmosphere to the Leakage of Photospheric Motion. *Sol. Phys.*258, 219–241.
- Fleck, B., Schmitz, F., Oct. 1991. The 3-min oscillations of the solar chromosphere - A basic physical effect? *A&A*250, 235–244.
- Goedbloed, J., Poedts, S., 2004. *Principles of Magnetohydrodynamics: With Applications to Laboratory and Astrophysical Plasmas*. Cambridge University Press, Cambridge, UK.
URL <https://books.google.co.uk/books?id=FvM6rMJob-cC>

- Griffiths, M., Erdélyi, R., Fedun, V., 2017. Videos of Magnetohydrodynamics Simulations of Solar Atmosphere Wave Dynamics Generated by Solar Global Oscillating Eigenmodes.
- URL https://figshare.com/articles/Videos_of_Magnetohydrodynamics_Simulations_of_Solar_Atmosphere_Wave_Dynamics_Generated_by_Solar_Global_Oscillating_Eigenmodes/4818490
- Griffiths, M. K., Fedun, V., Erdélyi, R., 2015. A Fast MHD Code for Gravitationally Stratified Media using Graphical Processing Units: SMAUG. *Journal of Astrophysics and Astronomy* 36, 197–223.
- Hill, H. A., 1976. Talk on Solar Diameter Oscillations. *The Observatory* 96, 130–132.
- Ireland, J., McAteer, R. T. J., Inglis, A. R., 2015. Coronal Fourier Power Spectra: Implications for Coronal Seismology and Coronal Heating. *ApJ798*, 12.
- Jefferies, S. M., McIntosh, S. W., Armstrong, J. D., Bogdan, T. J., Cacciani, A., Fleck, B., 2006. Low-frequency magneto-acoustic waves in the solar chromosphere. In: Proceedings of SOHO 18/GONG 2006/HELAS I, Beyond the spherical Sun. Vol. 624 of ESA Special Publication. p. 16.1.
- Kalkofen, W., 2012. The Validity of Dynamical Models of the Solar Atmosphere. *Sol. Phys.* 276, 75–95.
- Kalkofen, W., Rossi, P., Bodo, G., Massaglia, S., 2010. Acoustic waves in a stratified atmosphere. IV. Three-dimensional nonlinear hydrodynamics. *A&A520*, A100.
- Khomenko, E., Calvo Santamaria, I., 2013. Magnetohydrodynamic waves driven by p-modes. *Journal of Physics Conference Series* 440 (1), 012048.
- Kosovichev, A. G., Zhao, J., 2016a. Reconstruction of Solar Subsurfaces by Local Helioseismology. In: Rozelot, J.-P., Neiner, C. (Eds.), *Lecture Notes in Physics*, Berlin Springer Verlag. Vol. 914 of *Lecture Notes in Physics*, Berlin Springer Verlag. pp. 25–41.

- Kosovichev, A. G., Zhao, J., 2016b. Solar-Cycle Evolution of Subsurface Flows and Magnetic Field, Presentation abstract. In: AAS/Solar Physics Division Meeting. Vol. 47 of AAS/Solar Physics Division Meeting. p. 7.09.
- Lamb, H., 1932. Hydrodynamics. Cambridge University Press, Cambridge, UK.
- Leenaarts, J., Carlsson, M., Hansteen, V., Gudiksen, B. V., 2011. On the minimum temperature of the quiet solar chromosphere. *A&A*530, A124.
- Leibacher, J. W., Stein, R. F., 1971. A New Description of the Solar Five-Minute Oscillation. *ApJ Letter* 7, 191–192.
- Leighton, R. B., 1960. In: Thomas, R. N. (Ed.), Aerodynamic Phenomena in Stellar Atmospheres. Vol. 12 of IAU Symposium. pp. 321–325.
- Lites, B. W., Kubo, M., Socas-Navarro, H., Berger, T., Frank, Z., Shine, R., Tarbell, T., Title, A., Ichimoto, K., Katsukawa, Y., Tsuneta, S., Suematsu, Y., Shimizu, T., Nagata, S., 2008. The Horizontal Magnetic Flux of the Quiet-Sun Internetwork as Observed with the Hinode Spectro-Polarimeter. *ApJ*672, 1237–1253.
- Malins, C., 2007. On transition region convection cells in simulations of $\{p\}$ -mode propagation. *Astronomische Nachrichten* 328, 752–755.
- Mathioudakis, M., Jess, D. B., Erdélyi, R., 2013. Alfvén Waves in the Solar Atmosphere. From Theory to Observations. 175, 1–27.
- McWhirter, R. W. P., Thonemann, P. C., Wilson, R., 1975. The heating of the solar corona. II - A model based on energy balance. *A&A*40, 63–73.
- Murawski, K., Zaqrashvili, T. V., 2010. Numerical simulations of spicule formation in the solar atmosphere. *A&A*519, 9.
- Pintér, B., Erdélyi, R., 2011. Effects of Magnetic Fields in the Solar Atmosphere on Global Oscillations. *Space Science Review* 158, 471–504.
- Roberts, B., Edwin, P. M., Benz, A. O., 1984. On coronal oscillations. *ApJ*279, 857–865.

- Roth, M., Franz, M., Bello González, N., Martínez Pillet, V., Bonet, J. A., Gandorfer, A., Barthol, P., Solanki, S. K., Berkefeld, T., Schmidt, W., del Toro Iniesta, J. C., Domingo, V., Knölker, M., 2010. Surface Waves in Solar Granulation Observed with SUNRISE. *ApJL*723, L175–L179.
- Shelyag, S., Fedun, V., Erdélyi, R., 2008. Magnetohydrodynamic code for gravitationally-stratified media. *A&A*486, 655–662.
- Taroyan, Y., Erdélyi, R., 2008. Global Acoustic Resonance in a Stratified Solar Atmosphere. *Sol. Phys.*251, 523–531.
- Thompson, M. J., 2006. Magnetohelioseismology. *Philosophical Transactions of the Royal Society of London Series A* 364, 297–311.
- Tóth, G., 1996. A General Code for Modeling MHD Flows on Parallel Computers: Versatile Advection Code. *Astrophysical Letters and Communications* 34, 245.
- Ulrich, R. K., 1970. The Five-Minute Oscillations on the Solar Surface. *ApJ*162, 993–1002.
- Vernazza, J. E., Avrett, E. H., Loeser, R., 1981. Structure of the solar chromosphere. III - Models of the EUV brightness components of the quiet-sun. *Astrophysical Journal Supplement Series* 45, 635–725.
- Wang, T., 2011. Standing Slow-Mode Waves in Hot Coronal Loops: Observations, Modeling, and Coronal Seismology. 158, 397–419.

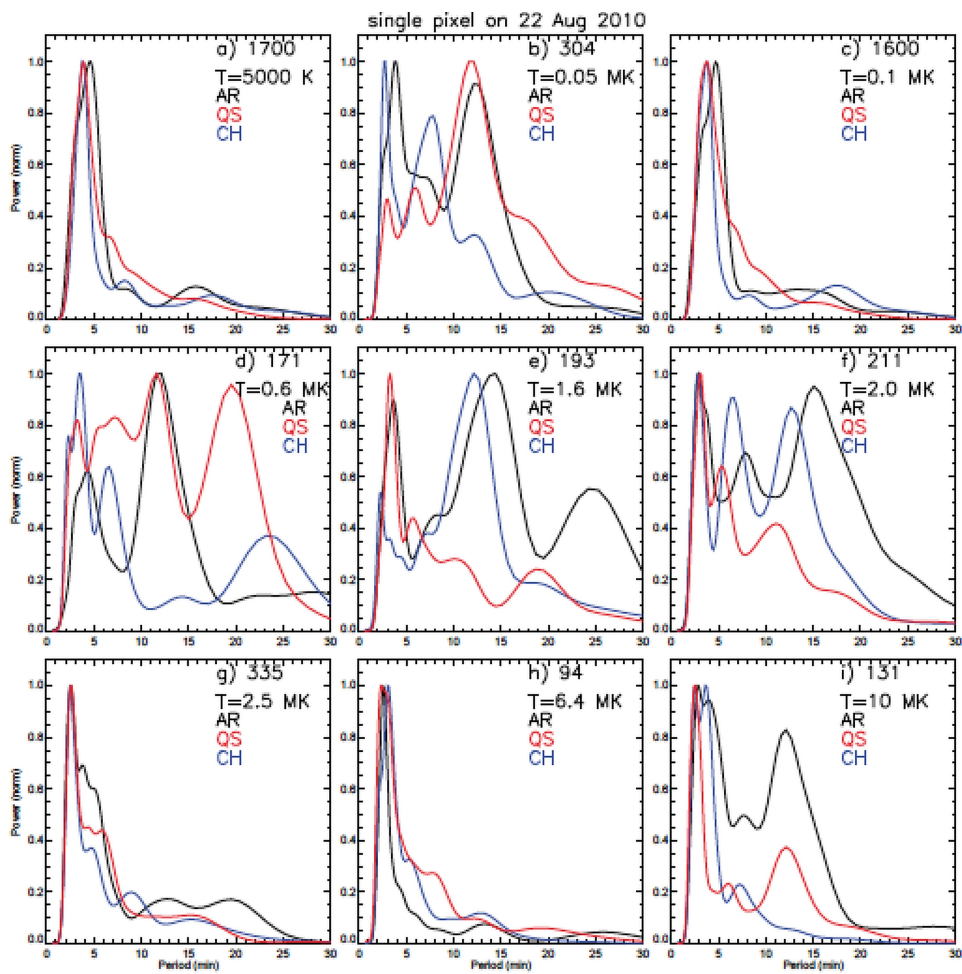


Figure 1: The power spectrum in nine AIA passbands for single pixels in AR (black solid), QS (red solid), and CH (blue solid).

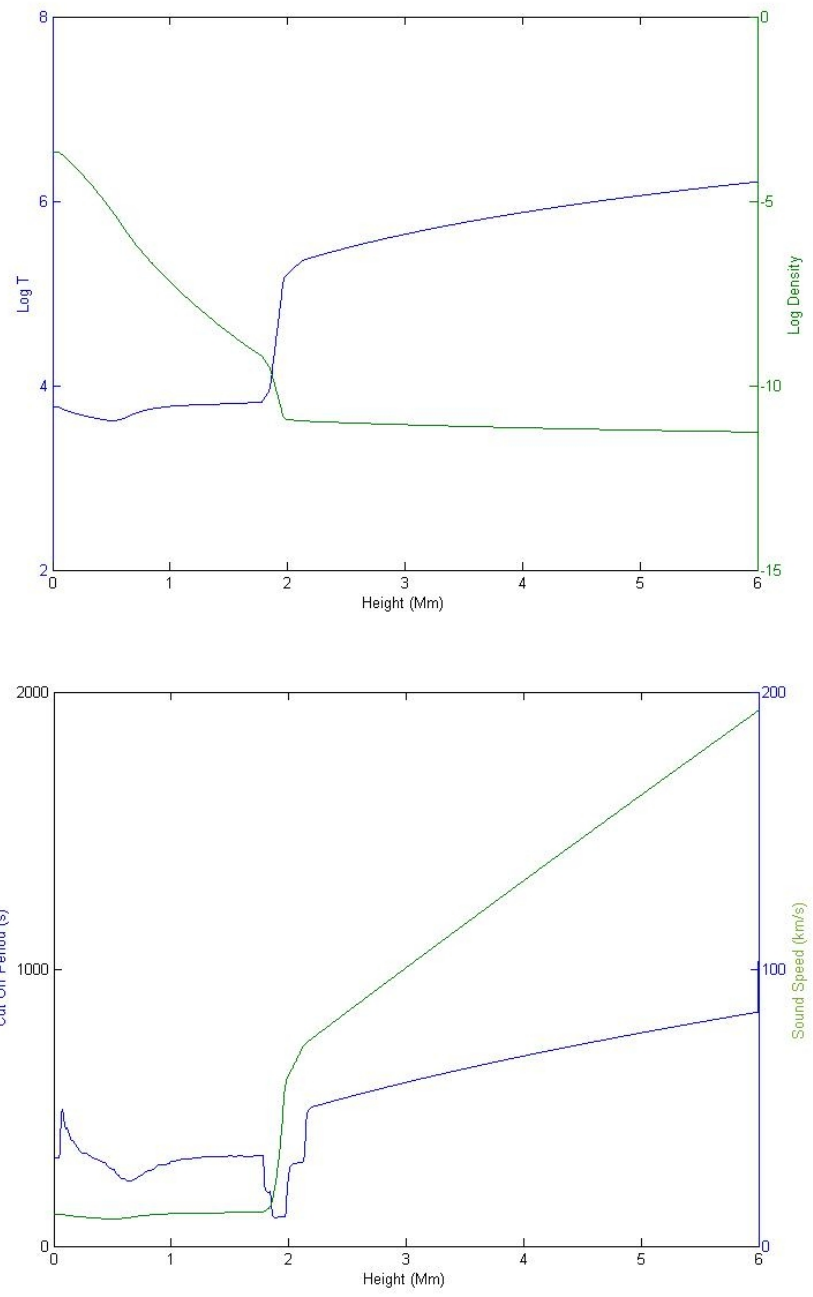


Figure 2: Temperature and density profiles (left) used for the model atmosphere and cut-off frequency at different heights (right).

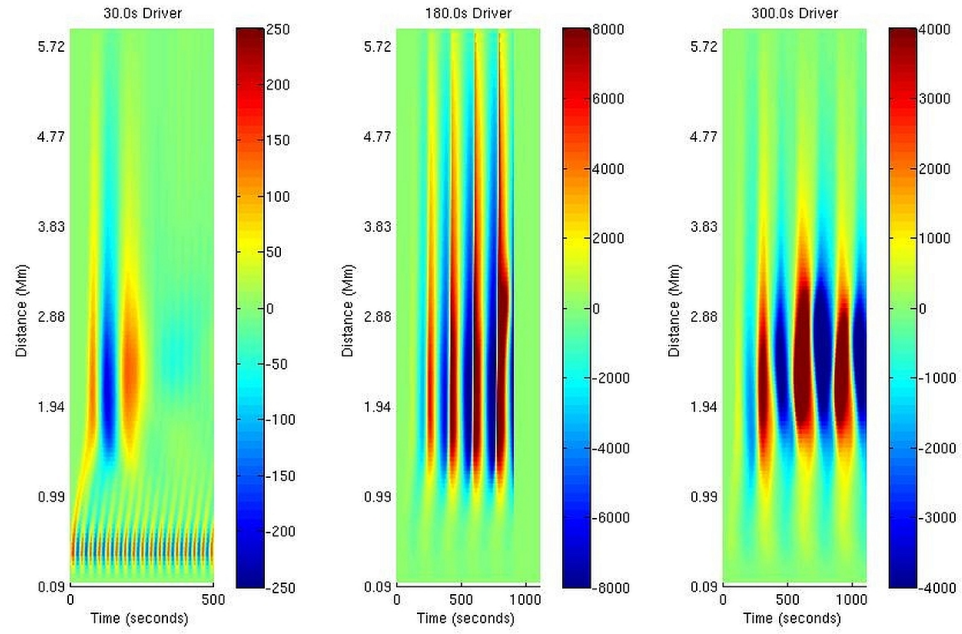


Figure 3: Time-distance plot for the fundamental mode $(0, 0)$ and 30, 180 and 300 s driver period for the z component of the velocity for a vertical slice across the box taken at 2 Mm and shows the profile of v_z through the solar atmosphere for different time steps (the left hand plot shows the case for the 30 s driver, the centre plot the case for the 180 s driver and the right hand plot shows the case for the 300 s driver). The colour bar shows the magnitude of v_z in $m s^{-1}$.

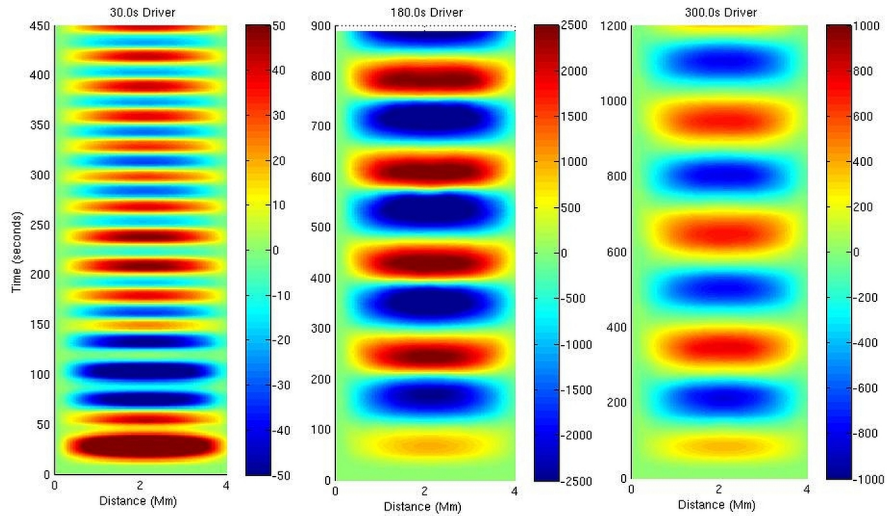


Figure 4: Time-distance plot for the fundamental mode $(0, 0)$ and 30, 180 and 300 s driver period for the z component of the velocity for a horizontal slice across the box taken at 0.94 Mm shows the profile of v_z across the simulation box at a given point (left hand is 30 s driver, centre is 180 s driver and the right hand is the 300 s driver). The colour bar shows the magnitude of v_z in $m s^{-1}$.

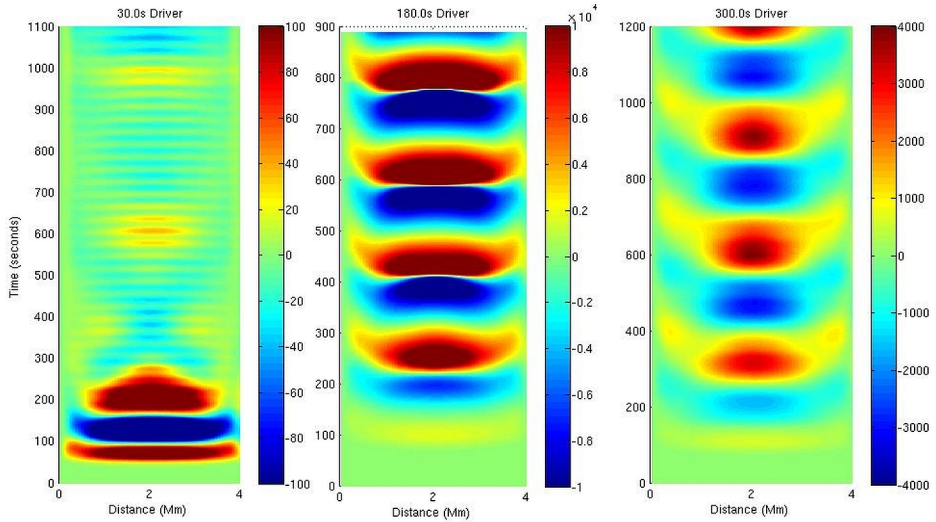


Figure 5: Time-distance plot for the fundamental model and 30, 180 and 300 s driver period for the z component of the velocity for a horizontal slice across the box taken at the transition zone shows the profile of v_z across the simulation box at a height of 2 Mm (left hand is 30 s driver, centre is 180 s driver and the right hand is the 300 s driver). The colour bar shows the magnitude of v_z in $m s^{-1}$.

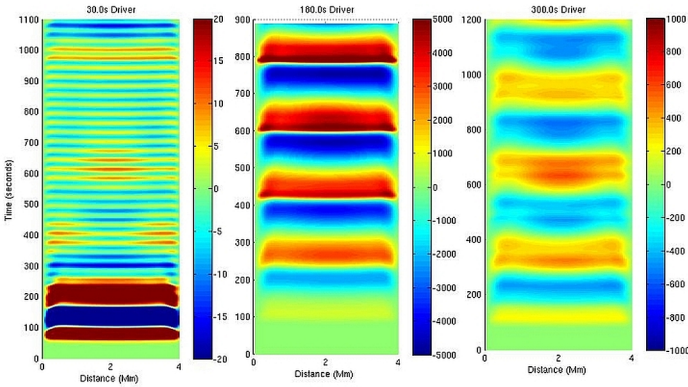


Figure 6: Time-distance plot for the fundamental mode and 30, 180 and 300 s driver period for the z component of the velocity for a horizontal slice across the box taken at 4.2 Mm shows the profile of v_z across the simulation box (left hand is 30 s driver, centre is 180 s driver and the right hand is the 300 s driver). The colour bar shows the magnitude of v_z in $m s^{-1}$.

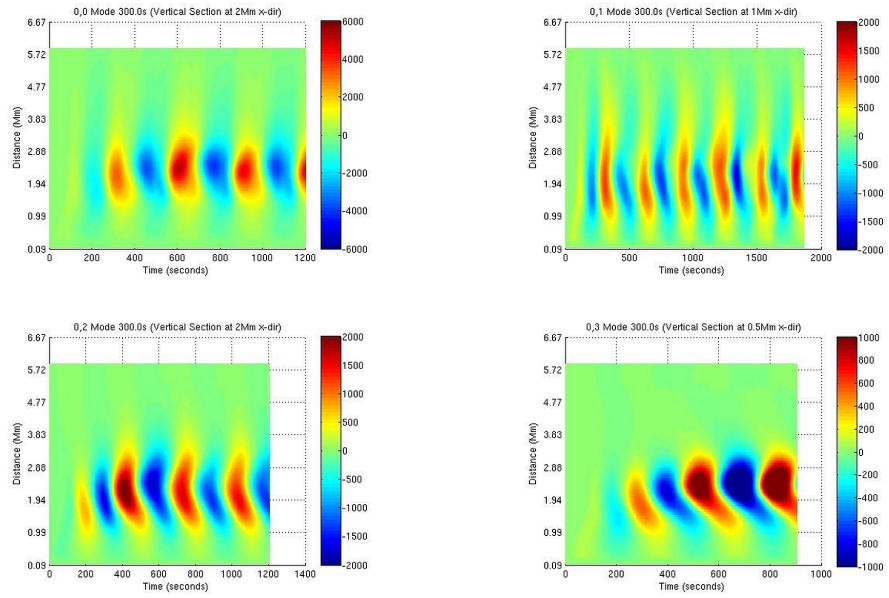


Figure 7: Time-distance plot for the fundamental mode with the 300 s period for the z component of the velocity, x -direction. The colour bar shows the magnitude of v_z in ms^{-1} .

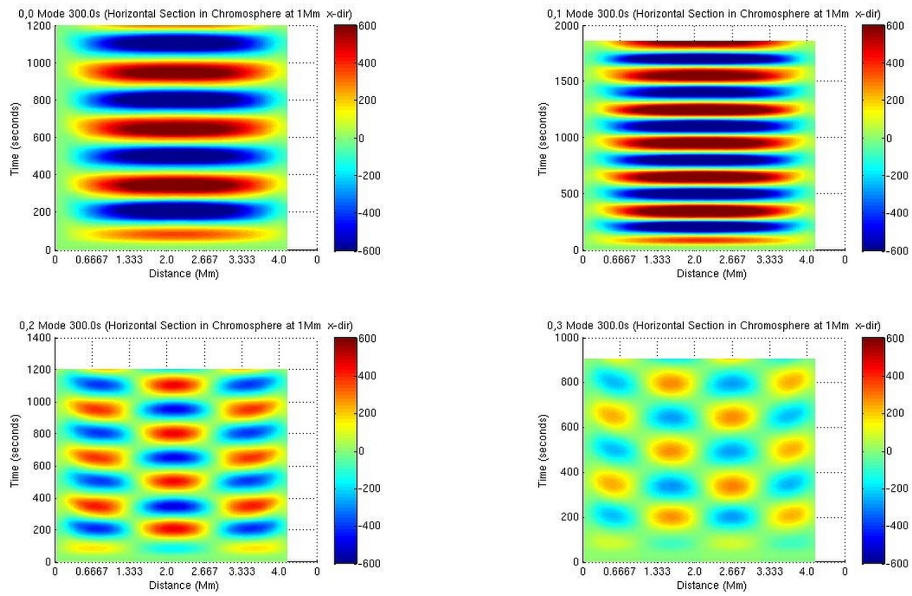


Figure 8: Time-distance plot for modes with 300 s period horizontal section through the chromosphere (at 1 Mm) for the z component of the velocity, x -direction. The colour bar shows the magnitude of v_z in ms^{-1} .

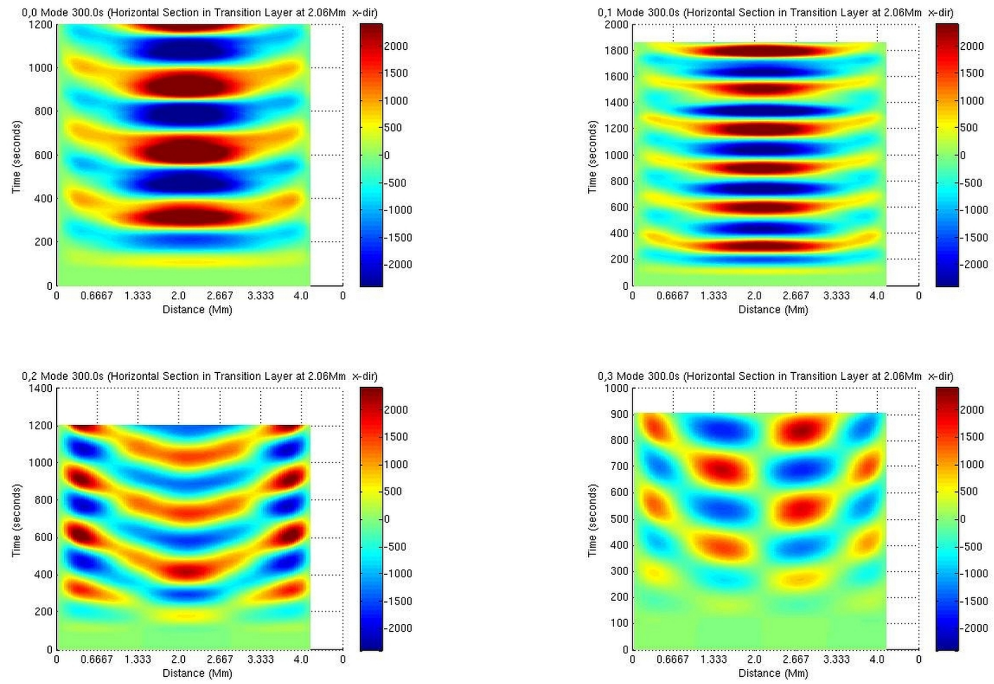


Figure 9: Time-distance plot for modes with 300 s period, horizontal section through the Transition Region (at 2.06 Mm) for the z component of the velocity, x -direction. The colour bar shows the magnitude of v_z in $m s^{-1}$.

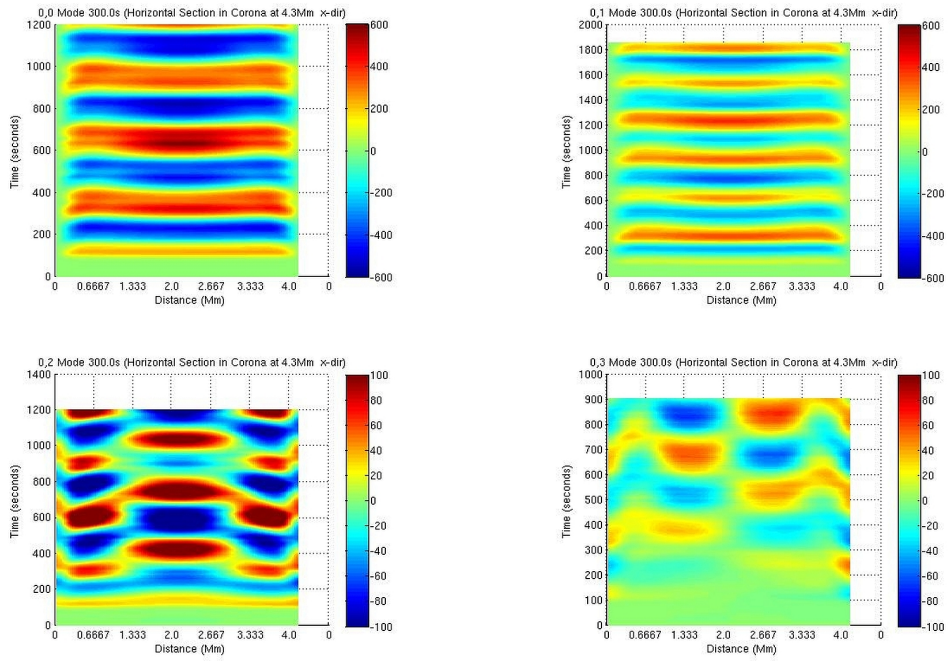


Figure 10: Time-distance plot for modes with 300 s period Horizontal Section through the Solar Corona (at 4.3 Mm) for the z component of the velocity, x -direction. The colour bar shows the magnitude of v_z in ms^{-1} .

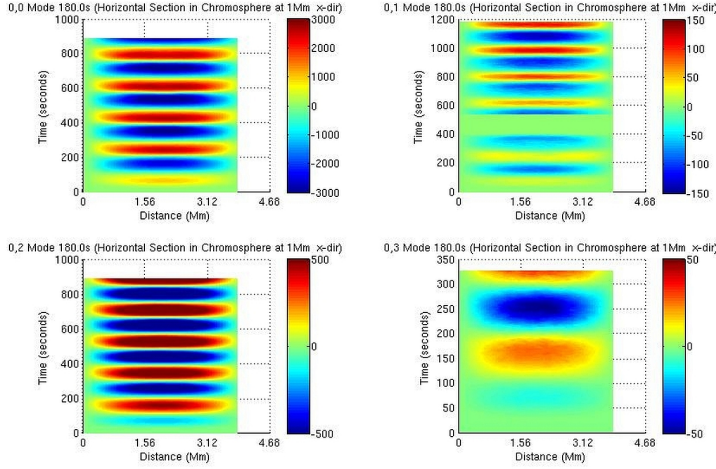


Figure 11: Time-distance plot for modes with 180 s period Horizontal Section through the Chromosphere (at 1 Mm) for the z component of the velocity, x -direction. The colour bar shows the magnitude of v_z in $m s^{-1}$.

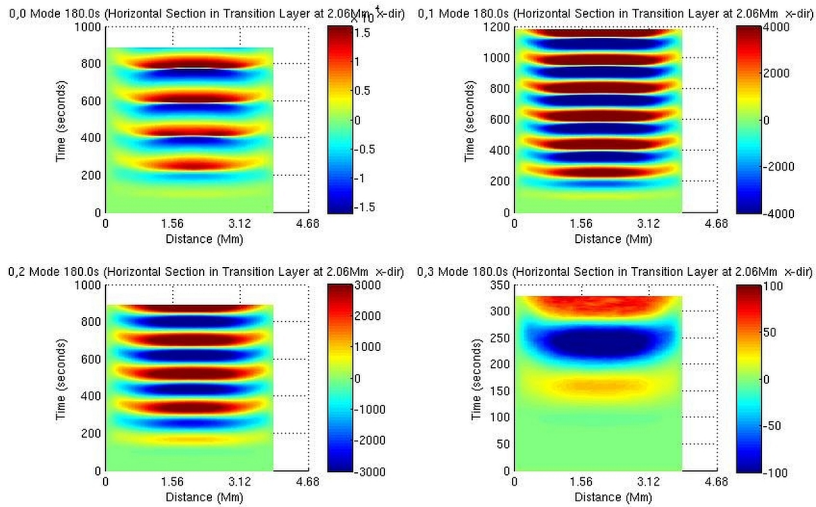


Figure 12: Time-distance plot for modes with 180 s period Horizontal Section through the Transition Region (at 2.06 Mm) for the z component of the velocity, x -direction. The colour bar shows the magnitude of v_z in $m s^{-1}$.

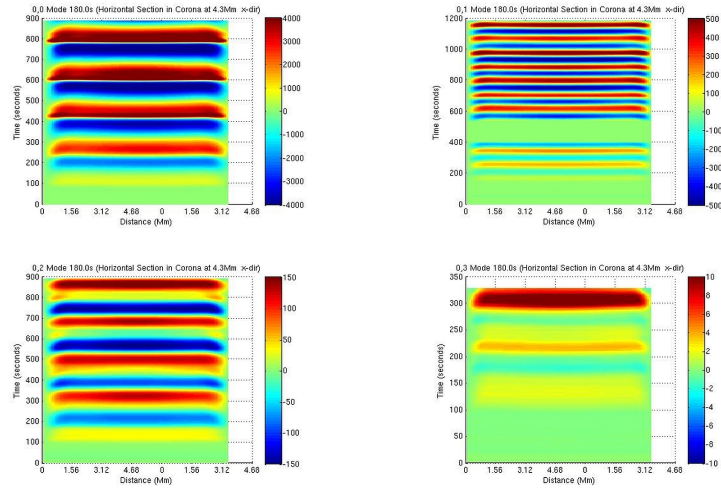


Figure 13: Time-distance plot for modes with 180 s period Horizontal Section through the Solar Corona (at 4.3 Mm) for the z component of the velocity, x -direction. The colour bar shows the magnitude of v_z in ms^{-1} .

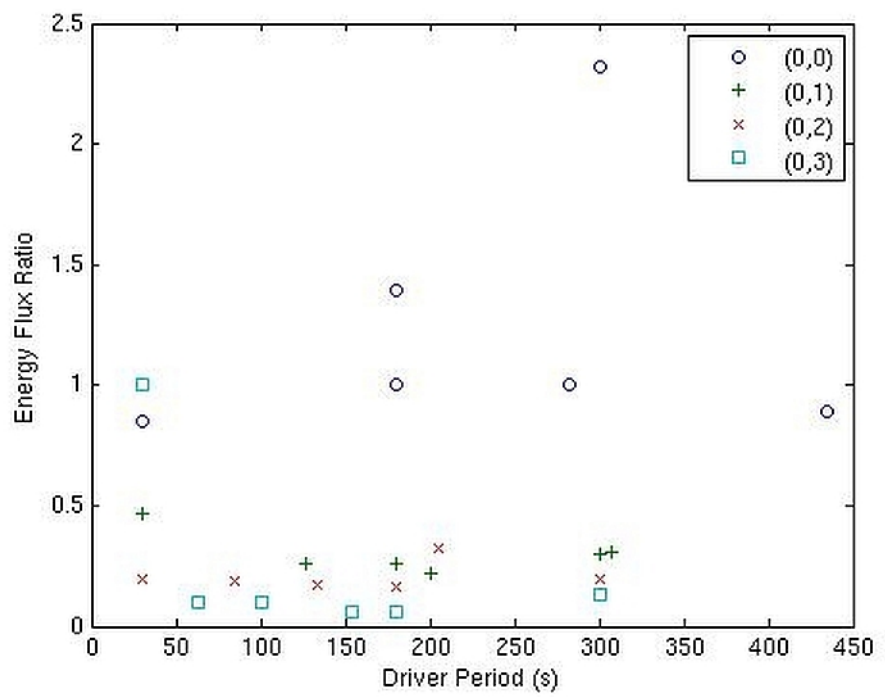


Figure 14: Variation of energy flux ratio at height of 5.5 Mm for a solar atmosphere excited with a p -mode driver providing the same amount of energy for all driver modes and periods

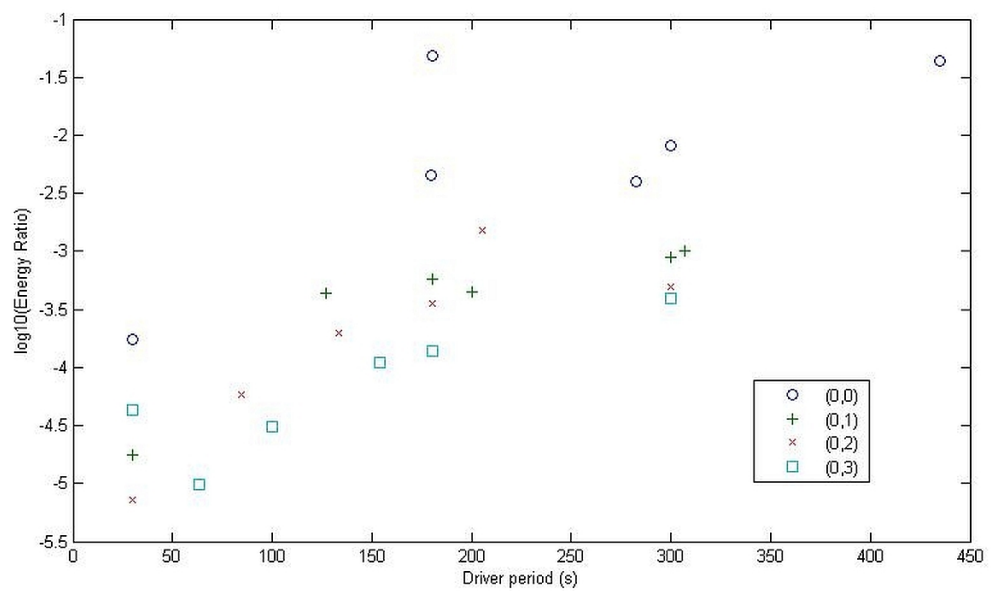


Figure 15: Variation of energy flux ratio with the driver energy at height of 5.5 Mm for a solar atmosphere excited with a p -mode driver of fixed amplitude

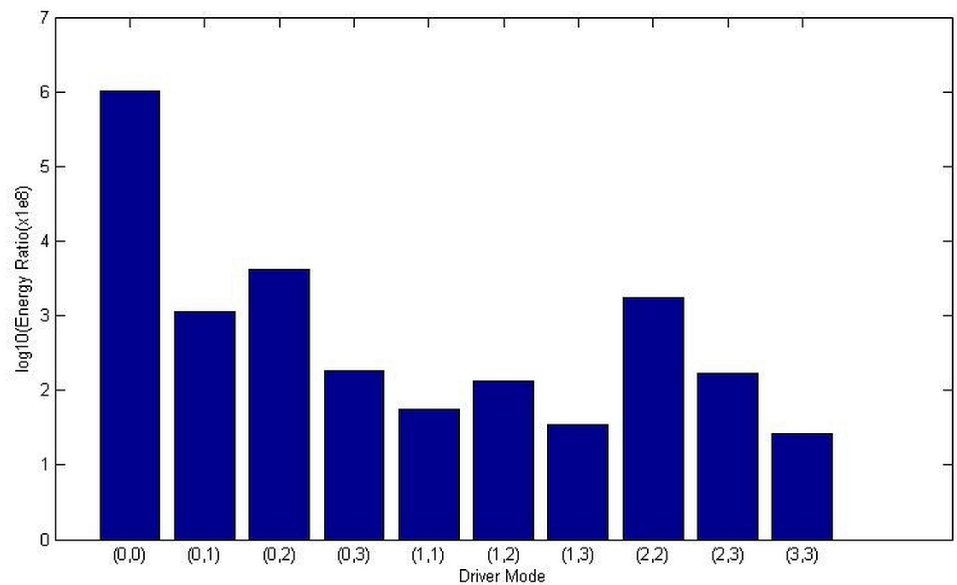


Figure 16: Variation of energy flux ratio at a height of 5.5 Mm for a solar atmosphere excited with 180 s p -mode driver located at height of 50 km

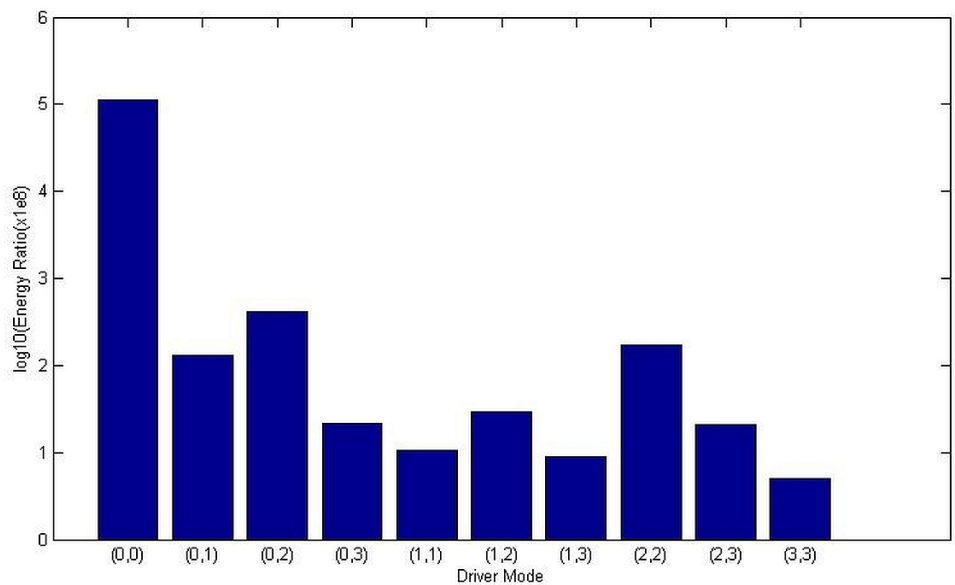


Figure 17: Variation of energy flux ratio at height of 5.5 Mm for a solar atmosphere excited with a 300 s *p*-mode driver located at a height of 50 km

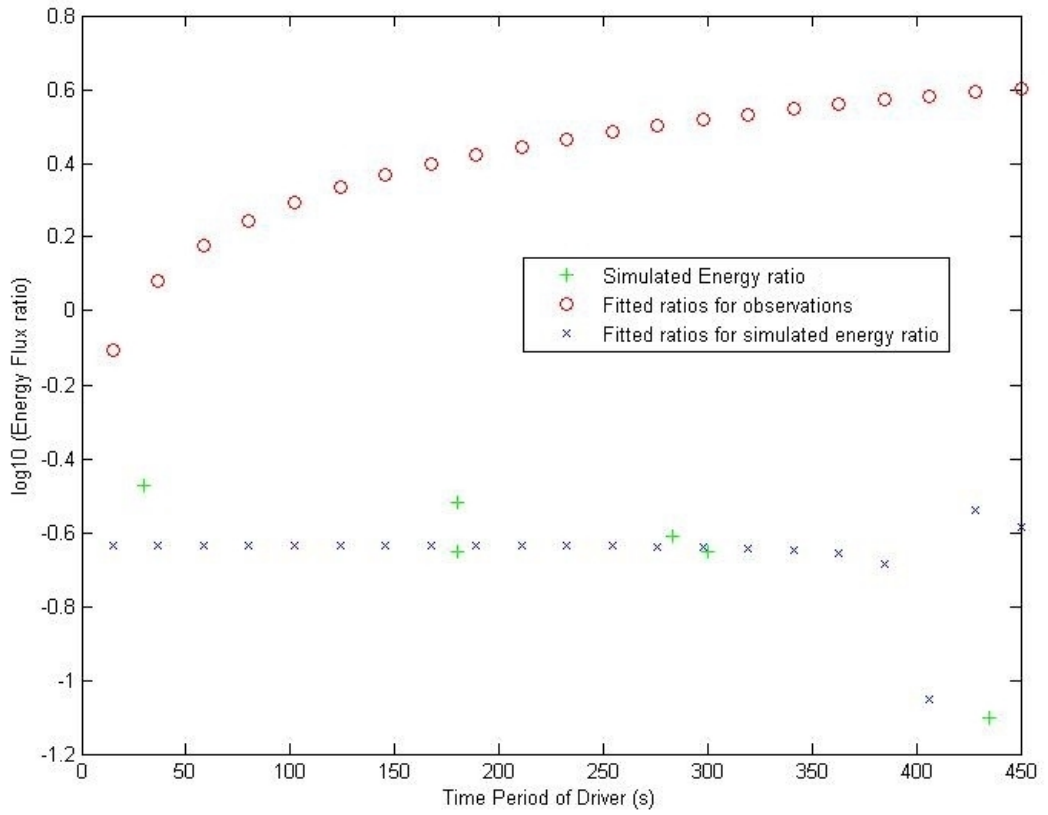


Figure 18: Comparison of the energy flux ratio for the $(0, 0)$ -mode with the observational power law ratio from the results of Ireland et al. (2015). For the simulation results we compute the ratio of the energy flux at $5.5Mm$ to the energy flux at $2Mm$. For the observational data we compute the ratio of the power laws for the results at 171\AA and the results at 193\AA .